

Description of Medium-Range Order in Amorphous Structures by Persistent Homology

Takenobu Nakamura,¹ Yasuaki Hiraoka,² Akihiko Hirata,¹
Emerson G. Escobar,³ Kaname Matsue,⁴ and Yasumasa Nishiura¹

¹WPI-AIMR, Tohoku University, Japan*

²Institute of Mathematics for Industry, Kyushu University, Japan[†]

³Graduate School of Mathematics, Kyushu University, Japan

⁴The Institute of Statistical Mathematics, Japan

(Dated: May 23, 2022)

The description of amorphous structures has been a long-standing problem, and conventional methods are insufficient for revealing intrinsic structures. In this Letter, we propose a computational homological approach that provides indicators of amorphous structures. We found curves in the persistence diagram (PD), which describes shapes and scales of medium-range order (MRO). The presence of such curves explicitly indicates geometric constraints on amorphous structures, which have not been observed using conventional methods. Furthermore, the PD reproduces the wavelength of the first sharp diffraction peak (FSDP) observed in the structure factor and clarifies the real space origin of FSDP. These curves are preserved under strain, indicating that PDs also contain information on elastic response.

PACS numbers: 61.43.Er, 61.43.Fs, 02.40.Re

Keywords: Amorphous Structure, Medium-Range Order, Persistence Diagram, Computational Homology

Introduction: The atomic structures of amorphous solids are difficult to characterize. Because the structure of amorphous solids has no periodicity as found in crystalline solids, only the local structure has been analyzed in detail. Although our current understanding of short-range order (SRO) defined by the nearest neighbors is satisfactory, it is not sufficient to characterize amorphous solids. Therefore, medium-range order (MRO) has been discussed to characterize amorphous structures properly [1–3]. Many experimental and simulation studies [4–7] have suggested signatures of MRO such as the first sharp diffraction peak (FSDP) in the structure factor. However, in contrast to SRO, the geometric interpretation of MRO is not yet clear.

Among the available methods, the distributions of bond angle and dihedral angle have been used to identify the geometry of MRO. However, because these distributions only extract the atomic configuration up to the third nearest neighbors, they cannot provide a complete description of MRO. Alternatively, as a conventional topological method, ring statistics [8–15] are often applied to materials described by the continuous random network model [2, 16]. Although this method is widely used for MRO, it does not accurately capture geometric structures. Therefore, methodologies that precisely characterize MRO are highly desired to understand the atomic structures of amorphous solids.

In recent years, computational homology [17], especially persistent homology, has provided us with tools for systematically characterizing geometric objects in physical and biological sciences [18–21]. A particularly important tool in computational homology is the persistence diagram (PD), which is a compact expression of the

persistent homology visualized as a two-dimensional histogram (see Fig. 1). Like the standard topological tools, PDs qualitatively capture topological properties such as rings. Moreover, a powerful and unique feature of PDs is the ability to provide the metrics of these properties. Hence, PDs can be used to classify topological properties by their scales and clarify the relationships among them; this is presumably the most desired function for further analysis of amorphous solids.

In this Letter, we propose a new method for the geometric characterization of amorphous silica, one of the most common network glasses, by using PDs. Our main results are as follows: (1) We found three characteristic curves in the PD of amorphous silica. (2) These curves describe the geometric properties of both tetrahedrons (SRO) and rings (MRO), and we revealed a hierarchical geometric relationship among them. In particular, the ring distribution defined by the PD reproduces the wavelength of the FSDP. (3) Each curve represents geometric constraints on and variations in the shapes of rings. Moreover, these curves are preserved under strain, suggesting that PDs properly encode the material properties concerning elastic response.

Persistence diagrams of silica: The input to persistent homology is a pair $\mathcal{A} = (Q, R)$ of an atomic configuration $Q = (\mathbf{x}_1, \mathbf{x}_2, \dots, \mathbf{x}_N)$ and a parameter set $R = (r_1, r_2, \dots, r_N)$. Here, \mathbf{x}_i and r_i are the position in \mathbb{R}^3 and the input radius for the i th atom, respectively. In order to characterize the multi-scale properties in Q , we introduce a parameter α , which controls resolution, and generate a family of atomic balls $B_i(\alpha) = \{\mathbf{x} \in \mathbb{R}^3 \mid \|\mathbf{x} - \mathbf{x}_i\| \leq r_i(\alpha)\}$ with the i th atom having the radius $r_i(\alpha) = \sqrt{\alpha + r_i^2}$. We increase the radii

of the atomic balls by changing α and extract topological features at each resolution. Let c_k be a ring in the atomic ball model $\bigcup_{i=1}^N B_i(\alpha)$. Then, we observe that there is a value $\alpha = b_k$ ($\alpha = d_k$) at which the ring c_k first appears (disappears) in the atomic ball model. The values b_k and d_k are called the birth and death scales of the ring c_k , respectively, and the collection of all these birth and death scales $(b_k, d_k) \in \mathbb{R}^2$ is called the persistence diagram $D_1(\mathcal{A})$ for \mathcal{A} . From this construction, the birth and death scales (b_k, d_k) encode some metric properties of the ring c_k . For example, b_k indicates the maximum distance between two adjacent atoms in c_k , whereas d_k indicates the size of c_k (see the supplementary material or [17] for details).

Fig. 1 shows the PDs $D_1(\mathcal{A}_{\text{liq}})$, $D_1(\mathcal{A}_{\text{amo}})$, and $D_1(\mathcal{A}_{\text{cry}})$ of a liquid $\mathcal{A}_{\text{liq}} = (Q_{\text{liq}}, R_{\text{liq}})$, an amorphous $\mathcal{A}_{\text{amo}} = (Q_{\text{amo}}, R_{\text{amo}})$, and a crystalline $\mathcal{A}_{\text{cry}} = (Q_{\text{cry}}, R_{\text{cry}})$ state, respectively. Here, the horizontal and vertical axes are the birth and death scales, respectively, and the histograms are plotted on a double-logarithmic scale. The configurations Q_{liq} , Q_{amo} and Q_{cry} are acquired by molecular dynamics (MD) simulations using the BKS model [22, 23]. The liquid configuration Q_{liq} is obtained after equilibration at 7000 K and 1 bar. Then, starting from this liquid state, the amorphous configuration Q_{amo} is obtained by linearly decreasing the temperature to 10 K [24]. Starting from beta-cristobalite structure, the crystalline configuration Q_{cry} is obtained after equilibration at 10 K and 1 bar. The input radii R are set to be $r_{\text{O}} = 1.275 \text{ \AA}$ and $r_{\text{Si}} = 0.375 \text{ \AA}$ for each type of the atom (O or Si), as determined by the first peak positions of the partial radial distribution functions of the amorphous configuration Q_{amo} . The details of the MD simulations and input radii are given in the supplementary material.

We discovered that the persistence diagrams $D_1(\mathcal{A}_{\text{liq}})$, $D_1(\mathcal{A}_{\text{amo}})$, and $D_1(\mathcal{A}_{\text{cry}})$ in Fig. 1 characterize the three states. The liquid, amorphous, and crystalline states are characterized by planar (2-dim), curvilinear (1-dim), and island (0-dim) regions, respectively. Here, the 0- and 2-dimensionality of the persistence diagrams result from the periodic and random atomic configurations of the crystalline and liquid states, respectively. Furthermore, we emphasize that the presence of the curves in $D_1(\mathcal{A}_{\text{amo}})$ clearly distinguishes the amorphous state from the others. This implies that specific geometric features of the rings generating the curves in $D_1(\mathcal{A}_{\text{amo}})$ play a significant role for elucidating amorphous structures.

The persistence diagram $D_1(\mathcal{A}_{\text{amo}})$ contains three characteristic curves, C_{P} , C_{T} , and C_{O} , and one band region, B_{O} , as shown in the figure. Through further analysis of the persistent homology, we found the following three geometric characterizations. (i) The rings on C_{P} secondarily generate those on C_{T} , C_{O} , and B_{O} (P is named after *primary*). That is, by increasing the parameter α , each ring on C_{P} becomes thicker and starts

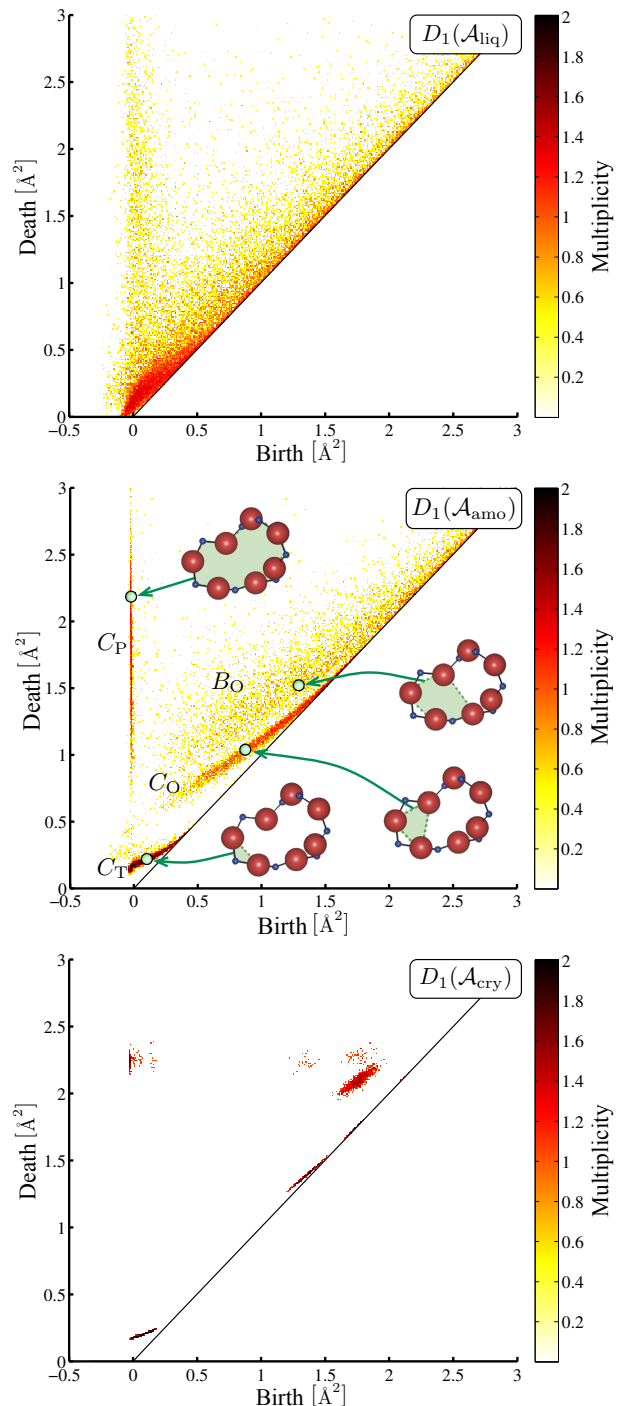


FIG. 1. Persistence diagrams of the liquid (top), amorphous (middle), and crystalline (bottom) states with the double-logarithmic scale of multiplicity. In the amorphous state, the three characteristic curves and one band region are labeled C_{P} , C_{T} , C_{O} , and B_{O} , respectively. The insets in $D_1(\mathcal{A}_{\text{amo}})$ show rings in the hierarchical relationship, where the red and blue spheres represent oxygen and silicon atoms, respectively.

to create new rings by pinching itself, and these newly generated rings appear on C_{T} , C_{O} , and B_{O} (a schematic

illustration of the pinching process is described in Fig. 2 in the supplementary material). This indicates a hierarchical structure from C_P to C_T , C_O , and B_O . An example of the rings in this hierarchical relationship is depicted in the inset of $D_1(\mathcal{A}_{\text{amo}})$. (ii) The rings on C_T are constructed by the tetrahedrons consisting of four oxygen atoms at the vertices with one silicon atom at the center. (iii) The rings on C_O and B_O are constructed only by the oxygen atoms (three and more, respectively). Recalling that the death scale indicates the size of rings, the rings on C_T are classified as SRO, while those on C_P , C_O , and B_O are classified as MRO. We also remark that the definition of the rings in our analysis adopts the mathematically rigorous one established in algebraic topology (see [25]).

Decomposition of FSDP: We also found that the distributions of the rings on C_P , C_O , and B_O reproduce the wavelength of the FSDP fairly well. Recall that α is the parameter controlling the radius $r_i(\alpha) = \sqrt{\alpha + r_i^2}$ of the i th atomic ball $B_i(\alpha)$, and the death scale $\alpha = d_k$ indicates the size of the individual ring c_k . More precisely, the ring c_k disappears at $\alpha = d_k$ by being covered up in the atomic ball model $\bigcup_{i=1}^N B_i(\alpha)$. We also note that the death scales of the rings on C_P , C_O , and B_O are determined only by the oxygen atoms.

From the aforementioned argument, we define the size of the rings c_k on C_P , C_O and B_O as $\ell(d_k) = 2\sqrt{d_k + r_O^2}$ and obtain wavelength distributions

$$M_{D_i}(q) = \frac{1}{|D_i|} \sum_{(b_k, d_k) \in D_i} \delta\left(q - \frac{2\pi}{\ell(d_k)}\right),$$

where δ is the delta function. Here, $D_1 = C_P \cup C_O \cup B_O$, $D_2 = C_P$, $D_3 = C_O$, and $D_4 = B_O$, and $|D_i|$ is the number of the rings in D_i . Fig. 2 shows plots of $M_{D_i}(q)$ and the structure factor $S(q)$ around the FSDP. We found good agreement between the wavelength of the FSDP and the wavelength of $M_{D_1}(q)$, in contrast to the wavelengths of $M_{D_i}(q)$ ($i = 2, 3, 4$). This result indicates a decomposition of the FSDP. That is, the individual MRO regions (C_P , C_O , or B_O) in the PD are not sufficient to characterize the FSDP; rather, their combination is needed to reproduce the FSDP. It should also be emphasized that the same wavelength distributions $M_{D_i}(q)$ are derived from the configuration of the oxygen atoms only. This shows that the configuration of oxygen atoms plays a significant role in the FSDP. Furthermore, the wavelength distributions are quantitatively invariant under the choice of the input radius r_O , implying that our analysis using PDs does not contain any artificial ambiguity.

Curves and shape constraints: The presence of curves C_P , C_T , and C_O in $D_1(\mathcal{A}_{\text{amo}})$ clearly distinguishes the amorphous state from the crystalline and liquid states. We emphasize here that this characteristic property shows the constraints induced by the normal directions of these curves on the shapes of the rings. For example,

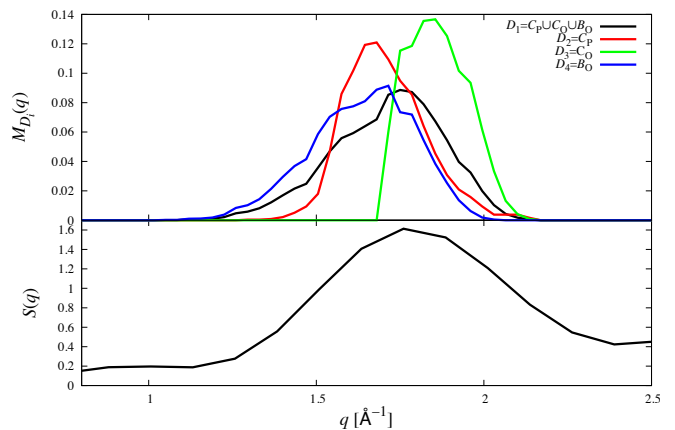


FIG. 2. The wavelength distributions $M_{D_i}(q)$ ($i = 1, 2, 3, 4$) and the structure factor $S(q)$ around the FSDP.

the shape of a ring on C_O , which consists of three oxygen atoms (see the inset in Fig. 3), is determined by specifying the first and second minimum edge lengths d_1 and d_2 ($d_1 < d_2$) and the angle θ between them. Then, the constraint for C_O to be the curve requires that these three variables (d_1, d_2, θ) satisfy some relation $f(d_1, d_2, \theta) = 0$. Fig. 3 shows a plot of (d_1, d_2, θ) for the O-O-O triangles on C_O in $D_1(\mathcal{A}_{\text{amo}})$, and we found a surface corresponding to this constraint $f(d_1, d_2, \theta) = 0$. This demonstrates one of the medium-range geometric structures in the amorphous state. It is worth noting that this new characterization of MRO expressed by both the lengths and angles of O-O-O triangles on C_O cannot be derived by separately analyzing the conventional distributions of lengths and angles.

This argument strongly relies on one of the striking features of PDs: descriptions with metric information of geometric structures in many-body configurations. This is in contrast to the conventional methods such as the pair correlation function (e.g., radial distribution function or structure factor) and ring statistics; the former does not directly describe many-body configurations, whereas the latter does not incorporate metric information. As we observed, the presence of curves or islands in PDs indicates nontrivial constraints in the geometric structures. These characteristic features indicate the signatures of orders in many-body configurations, and the birth/death coordinates in PDs provide the metric information of the orders.

Response under strain: The above argument about the shape constraints also shows that the presence of the curves indicates variations in ring configurations along the tangential directions. It is reasonable to suppose that these variations are due to thermal fluctuations, and hence the deformations of the ring configurations along the curves are probably softer than those in the normal directions. Consequently, the response under strain is

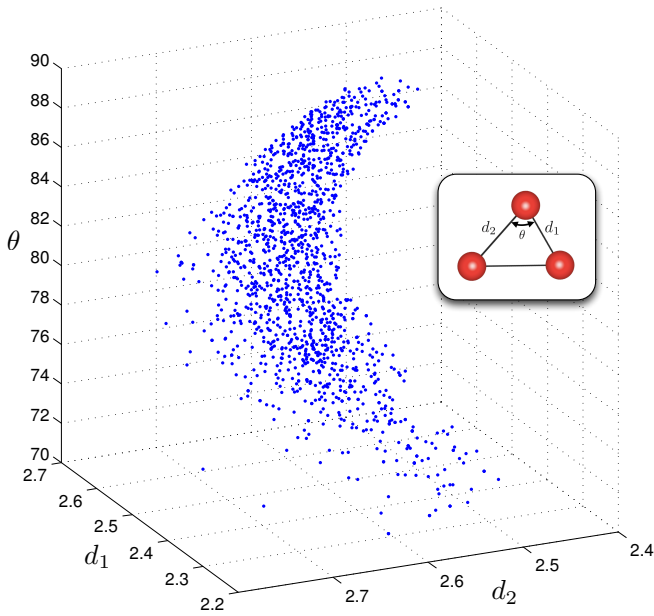


FIG. 3. Plot of (d_1, d_2, θ) for the O-O-O triangles on C_0 . The presence of the surface shows an MRO geometric structure in amorphous silica

expected to follow the same shape constraints.

To verify this mechanical response of PDs, we performed simulations of isotropic compression for our amorphous state, and we computed the PD of the strained state. The strain is set to be 1% in the original volume, which is sufficiently small to satisfy a linear response relation with the stress. Fig. 4 shows the contours of C_P , C_O , and C_T for the original configuration Q_{amo} of the amorphous state, for the strained state $Q_{\text{amo}}^{\text{strain}}$, and for the artificial 1% linear shrink of the original coordinates $Q_{\text{amo}}^{\text{linear}}$, respectively. The contours of C_O are depicted on the coordinates along the tangential direction.

The figures show that the contours of the strained state move along the original curves C_P , C_O , and C_T in $D_1(\mathcal{A}_{\text{amo}})$; i.e., downward in C_P , leftward in C_O , and almost fixed in C_T , respectively. This is in contrast to the linear shrink, in which the contours simply move in the direction of decreasing birth and death scales because of the effect of the uniform shrink of the system size. This strongly suggests that the configuration $Q_{\text{amo}}^{\text{strain}}$ reflects the shape constraints much better than $Q_{\text{amo}}^{\text{linear}}$, and supports the expected mechanical response of PDs. We also note from the figures of $Q_{\text{amo}}^{\text{strain}}$ that the contour of C_T is almost fixed compared with those of C_P and C_O . Since C_P and C_O (C_T) are classified as MRO (SRO), this implies that SRO is mechanically more rigid than MRO. Here, we remark that on using the same analysis for a shear deformation instead of isotropic compression, we can observe a similar behavior of the PDs under the strain.

We have revealed that PDs accurately encode infor-

mation about elastic response, similar to how the radial distribution function encodes the volume compressibility [26]. It should also be emphasized that the curves or islands only appear in the PDs of the solids. This evidence suggests that these isolated regions are related to the rigidity of the materials. This hypothesis follows from the fact that isolations represent geometric constraints reflecting mechanical responses. Future numerical and theoretical studies to unravel this relationship would be of great value.

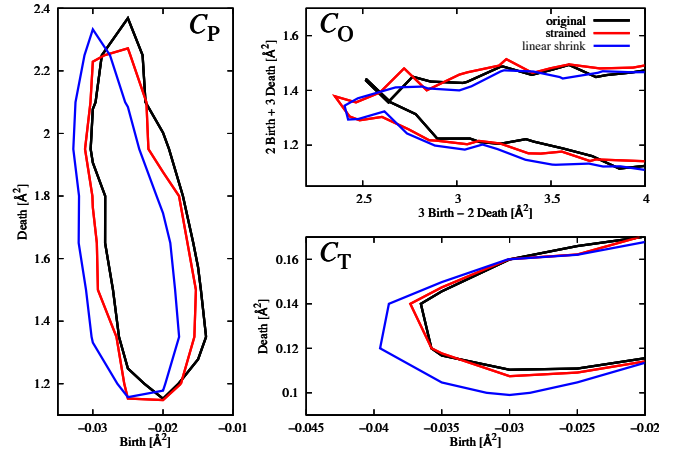


FIG. 4. Contour plots of C_P , C_O , and C_T representing the original configuration Q_{amo} of the amorphous state (black), the 1% strained state $Q_{\text{amo}}^{\text{strain}}$ (red), and the artificial 1% linear shrink of the original coordinates $Q_{\text{amo}}^{\text{linear}}$ (blue), respectively. The contours of C_O are depicted on the coordinates along the tangential direction.

Conclusion: We have presented a new technique for characterizing amorphous structures. The amorphous state is well characterized by the existence of curves in the PDs, in addition to the island and planar regions for crystalline and liquid states, respectively. Compared with existing tools, the PDs of the amorphous state clearly represent MRO through the curves C_P and C_O and the band region B_O , and we have shown that C_P , C_O , and B_O reproduce and decompose the wavelength of the FSDP. Furthermore, we have revealed a hierarchical structure embedded in MRO. We have also demonstrated that the curves C_P , C_O , and C_T show geometric constraints on the rings and that they encode mechanical properties of the materials. It should be emphasized that the proposed method is not restricted to network-forming materials. Hence, it is of great interest to apply PDs to other structurally disordered materials such as metallic glasses, molecular liquids, colloidal glasses, and highly concentrated granular materials in order to further elucidate their rich geometric structures.

T.N. and Y.H. contributed equally to this work. We thank Mingwei Chen, Hajime Tanaka, Masakazu Matsumoto, and Daniel Miles Packwood for valuable discus-

sions and comments. This work was sponsored by “WPI Research Center Initiative for Atoms, Molecules and Materials,” Ministry of Education, Culture, Sports, Science and Technology of Japan. Y.H. is supported by JSPS 26610042. K.M. is supported by “MEXT, Coop With Math Program.” Y.N. is supported by JSPS 26310205.

* t.nakamura@wpi-aimr.tohoku.ac.jp

† hiraoka@imi.kyushu-u.ac.jp

- [1] J. Bernal, Proc. R. Soc. A **280**, 299 (1964).
- [2] D. E. Polk, J. Non-Crystalline Solids **5**, 365 (1971).
- [3] Proc. Roy. Soc. Lond. A. **319**, 479 (1970).
- [4] S. R. Elliott, Phys. Rev. Lett. **67**, 1477 (1991).
- [5] S. R. Elliott, *Physics of Amorphous Material* (Longman, 1990), 2nd ed.
- [6] S. Susman, K. J. Volin, D. L. Price, M. Grimsditch, J. P. Rino, R. K. Kalia, P. Vashishta, G. Gwanmesia, Y. Wang, and R. C. Liebermann, Phys. Rev. B **43**, 1194 (1991).
- [7] G. N. Greaves and S. Sen, Adv. Phys. **56**, 1 (2007).
- [8] S. V. King, Nature **213**, 1112 (1967).
- [9] L. Guttman, J. Non-Cryst. Solids **116**, 145 (1990).
- [10] C. S. Mariani and L. W. Hobbs, J. Non-Cryst. Solids **124**, 242 (1990).
- [11] L. W. Hobbs, C. E. Jesurum, V. Pulim, and B. Berger, Philos. Mag. A **78**, 679 (1998).
- [12] D. S. Franzblau, Phys. Rev. B **44**, 4925 (1991).
- [13] K. Goetzke and H. J. Klein, J. Non-Cryst. Solids **127**, 215 (1991).
- [14] X. Yuan and A. N. Cormack, Comput. Mater. Sci **24**, 343 (2002).
- [15] F. Wooten, Acta Cryst. A **58**, 346 (2002).
- [16] W. H. Zachariasen, J. Am. Chem. Soc. **54**, 3841 (1932).
- [17] H. Edelsbrunner and J. Harer, *Computational Topology: An Introduction* (Amer. Math. Soc. 2010).
- [18] G. Carlsson, Bull. Amer. Math. Soc. **46**, 255 (2009).
- [19] M. Gameiro, Y. Hiraoka, S. Izumi, M. Kramar, K. Mischaikow, and V. Nanda, to appear in Japan. J. Ind. Appl. Math.
- [20] A. Hirata, L. J. Kang, T. Fujita, B. Klumov, K. Matsue, M. Kotani, A. R. Yavari, and M. W. Chen, Science **341**, 376 (2013).
- [21] H. Kurtuldu, H. Kurtuldu, K. Mischaikow, and M. F. Schatz, Phys. Rev. Lett. **107**, 034503 (2011).
- [22] B. W. H. van Beest, G. J. Kramer, and R. A. van Santen, Phys. Rev. Lett. **64**, 1955 (1991).
- [23] Y. Guissani and B. Guillot, J. Chem. Phys. **104**, 7633 (1996).
- [24] K. Vollmayr, W. Kob, and K. Binder, Phys. Rev. B **54**, 15808 (1996).
- [25] A. Hatcher, *Algebraic Topology* (Cambridge University Press. 2001).
- [26] J.-P. Hansen and I. R. McDonald, *Theory of Simple Liquids* (Academic Press. 2006), 3rd ed.

Supplementary Material for “Description of Medium-Range Order in Amorphous Structures by Persistent Homology”

Takenobu Nakamura,¹ Yasuaki Hiraoka,² Akihiko Hirata,¹
Emerson G. Escolar,³ Kaname Matsue,⁴ and Yasumasa Nishiura¹

¹*WPI-AIMR, Tohoku University, Japan**

²*Institute of Mathematics for Industry, Kyushu University, Japan[†]*

³*Graduate School of Mathematics, Kyushu University, Japan*

⁴*The Institute of Statistical Mathematics, Japan*

(Dated: May 23, 2022)

Generating atomic configurations: MD simulations were performed to generate the atomic configurations Q_{liq} , Q_{amo} , and Q_{cry} of a liquid, an amorphous solid, and a crystalline solid, respectively. The system was composed of 2700 silicon atoms and 5400 oxygen atoms represented using the BKS silica model [1], and the 24-6 Lenard-Jones potential is assigned to correct for the unphysical behavior during equilibration in the liquid state [2]. Despite its simplicity, the BKS model reasonably reproduces the static and dynamic properties of amorphous silica [3, 4]. These MD simulations were performed using LAMMPS [5].

The liquid configuration Q_{liq} was generated by equilibrating the system from a random initial configuration for 50 ps at 1 bar and 7000 K, maintained using the Andersen barostat and the Nosé-Hoover thermostat, respectively. The step size was set to be 1.0 fs.

The amorphous configuration Q_{amo} was generated by cooling [3]. Starting from the liquid configuration at the heat-bath temperature $T_i = 7000$ K, the heat-bath temperature was decreased linearly as $T_b(t) = T_i - \gamma t$ to the final temperature $T_f = 10$ K with $\gamma = 10^{12}$ K/s. Throughout the cooling process, the barostat pressure was kept at 1 bar. At high temperatures of $1500 \text{ K} \leq T_b \leq 6000 \text{ K}$, we used the Anderson barostat with the damping parameter for the thermostat as $\tau_{\text{th}} = 1.0$ ps and that for the barostat as $\tau_{\text{bar}} = 1.0$ ps. At low temperatures of $10 \text{ K} \leq T_b \leq 1500 \text{ K}$, we used the Parrinello-Raman barostat with $\tau_{\text{th}} = 1.0$ ps and $\tau_{\text{bar}} = 0.5$ ps. Then, Q_{amo} was obtained as the final configuration of the cooling process. We tested five cooling rates, $\gamma = 10^{15}, 10^{14}, 10^{13}, 10^{12}, 10^{11}$ K/s, and checked that these choices do not affect our results qualitatively.

The crystalline configuration Q_{cry} was obtained with equilibration of the beta-cristobalite structure for 5 ps at 1 bar and 10 K, maintained using the Parrinello-Raman barostat and Nosé-Hoover thermostat with the damping parameters $\tau_{\text{bar}} = 0.5$ ps and $\tau_{\text{th}} = 0.8$ ps, respectively.

Generating the input radii: The set $R = (r_1, \dots, r_N)$ of input radii can be adjusted for each atom \mathbf{x}_i ($i = 1, \dots, N$). In our analysis, we chose the radii r_{Si} and r_{O} of silicon and oxygen using the first peak positions of the partial radial distribution functions of Q_{amo} . The peaks for SiO, OO, and SiSi were estimated as $d_{\text{SiO}} = 1.65 \text{ \AA}$, $d_{\text{OO}} = 2.55 \text{ \AA}$, and $d_{\text{SiSi}} = 3.15 \text{ \AA}$, respectively. Then, we selected the smallest two peaks and determined r_{Si} and r_{O} by solving $r_{\text{Si}} + r_{\text{O}} = d_{\text{SiO}}$ and $2r_{\text{O}} = d_{\text{OO}}$. This led to $r_{\text{O}} = 1.275 \text{ \AA}$ and $r_{\text{Si}} = 0.375 \text{ \AA}$.

Computational homology: We summarize the computational homological tools used

in this Letter. For further mathematical and computational details, please refer to [6].

Given a pair $\mathcal{A} = (Q, R)$ of an atomic configuration $Q = (\mathbf{x}_1, \mathbf{x}_2, \dots, \mathbf{x}_N)$ and a set $R = (r_1, r_2, \dots, r_N)$ of input radii, the persistence diagram captures hierarchical structures of the rings in a one-parameter family of alpha shapes $A(Q, R; \alpha)$. Here, the alpha shape $A(Q, R; \alpha)$ is constructed as follows. Let $\mathbb{R}^3 = \bigcup_{i=1}^N V_i$ be the Voronoi decomposition for Q , where V_i is the Voronoi cell of \mathbf{x}_i . For each parameter α , we assign a ball $B_i(\alpha) = \{\mathbf{x} \in \mathbb{R}^3 \mid \|\mathbf{x} - \mathbf{x}_i\| \leq r_i(\alpha)\}$ with the radius $r_i(\alpha) = \sqrt{\alpha + r_i^2}$ for the i th atom. Then, the alpha shape $A(Q, R; \alpha)$ is defined by the dual of the cut balls $C_i(\alpha) = V_i \cap B_i(\alpha)$, $i = 1, \dots, N$. This is a polyhedron with the vertex set Q such that an edge $|\mathbf{x}_i \mathbf{x}_j|$ (triangle, tetrahedron, respectively) is assigned to $A(Q, R; \alpha)$ if and only if the intersection $C_i(\alpha) \cap C_j(\alpha)$ of the corresponding double (triple, quadruple, respectively) cut balls is nonempty (see Fig. 1). In this Letter, the alpha shapes were computed using CGAL [7].

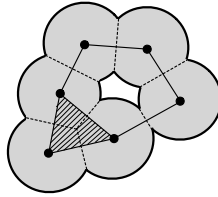


FIG. 1. Alpha shape.

One of the important properties of the alpha shape is that the atomic ball model $B(\alpha) = \bigcup_{i=1}^N B_i(\alpha)$ and the alpha shape $A(Q, R; \alpha)$ can be continuously deformed to each other. Hence, there is no loss of topological information in the use of the alpha shape model, which is much easier to analyze computationally than the atomic ball model. Furthermore, by changing the parameter α , we can trace the hierarchical structures of the rings in $B(\alpha)$. In other words, the parameter α controls the resolution from fine ($\alpha \approx 0$) to crude ($\alpha \gg 0$) geometric features.

Fig. 2 shows a schematic illustration of atomic ball models $B(\alpha)$ with the rings on C_P (red), C_T (blue), C_O (yellow), and B_O (green). Here, the large (small) balls correspond to oxygen (silicon). At each α_i ($i = 2, 3, 4, 5$), a new ring appears, and the dashed rings express the rings that have disappeared. The hierarchical ring structures are observed at α_3 , α_4 , and α_5 , at which new rings are generated by pinching the primary ring.

The persistence diagram is a two-dimensional histogram recording the birth and death

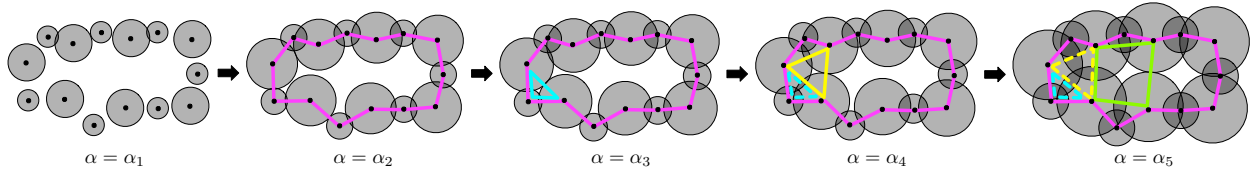


FIG. 2. Schematic illustration of atomic ball models $B(\alpha)$ showing the rings on C_P (red), C_T (blue), C_O (yellow), and B_O (green). Here, the large (small) balls correspond to oxygen (silicon). As we increase the parameter α , the primary ring generates the secondary rings in the hierarchy.

scales of the rings in a one-parameter family $\{B(\alpha)\}_\alpha$ of atomic ball models. For example, let c be the yellow ring in Fig. 2. We observe that c first appears at $\alpha = \alpha_4$ and first disappears at some value α_* , where $\alpha_4 < \alpha_* < \alpha_5$. Then, the birth and death scales b and d , respectively, of the ring c are determined by $b = \alpha_4$ and $d = \alpha_*$. The histogram of the birth and death pairs $(b, d) \in \mathbb{R}^2$ for all the rings appearing in the one-parameter family $\{B(\alpha)\}_\alpha$ is called the persistence diagram $D_1(\mathcal{A})$. Fig. 3 shows the persistence diagram of Fig. 2. From the definition of the persistence diagram, the birth scale indicates the maximum distance between adjacent atoms in the ring, whereas the death scale indicates the size of the ring. It should also be mentioned that persistence diagrams $D_i(\mathcal{A})$ can be similarly defined for any nonnegative integer $i \in \{0, 1, 2, \dots\}$, and they capture higher-dimensional topological features. The persistence diagrams can be computed, for example, using Perseus [8] or PHAT [9].

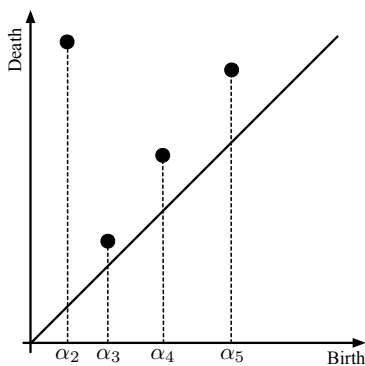


FIG. 3. The persistence diagram of Fig. 2.

* t.nakamura@wpi-aimr.tohoku.ac.jp

† hiraoka@imi.kyushu-u.ac.jp

- [1] B. W. H. van Beest, G. J. Kramer, and R. A. van Santen, *Phys. Rev. Lett.* **64**, 1955 (1991).
- [2] Y. Guissani and B. Guillot, *J. Chem. Phys.* **104**, 7633 (1996).
- [3] K. Vollmayr, W. Kob, and K. Binder, *Phys. Rev. B* **54**, 15808 (1996).
- [4] J. Horbach, W. Kob, and K. Binder, *J. Non-Cryst. Solids* **320**, 235 (1998).
- [5] S. Plimpton, *J. Comput. Phys.* **117**, 1 (1995).
- [6] H. Edelsbrunner and J. Harer. *Computational Topology: An Introduction* (Amer. Math. Soc. 2010).
- [7] CGAL webpage: <http://www.cgal.org/>
- [8] Perseus webpage: <http://www.math.rutgers.edu/~vidit/perseus.html>
- [9] PHAT webpage: <https://code.google.com/p/phat/>